JETIR.ORG ISSN: 2349-5162 | ESTD Year : 2014 | Monthly Issue

JOURNAL OF EMERGING TECHNOLOGIES AND INNOVATIVE RESEARCH (JETIR)

An International Scholarly Open Access, Peer-reviewed, Refereed Journal

# X RAY SPECTROSCOPIC STUDY OF TUNGSTEN COMPOUNDS

**Awad Kishore Singh[1], Dr. Vipin Kumar[2]**

[1]Research Scholar, OPJS University, Churu Rajasthan

[2]Research Supervisor, OPJS University, Churu Rajasthan

**Abstract**

X-ray absorption spectroscopy (XAS) is routinely used to probe the context of transition metal centres in biological systems. Studies involving co-ordination chemistry and X-ray absorption spectroscopy (XAS) are very complementary. Tungsten oxide has had its hydrogen intercalation into its monoclinic (m-WO3), metastable hexagonal (h-WO3), and cubic (c-WO3) phases investigated by in situ x-ray absorption fine structure (XAFS) (at the W L3-edge) and x-ray diffraction (XRD) methods. Using XAFS and XRD data, we were able to reconstitute the local environment surrounding tungsten ions in their initial coordination shell. The outcomes are contrasted with those predicted by currently available structural models. When there is no coordinated water present, the XANES spectra reveals that the surface tungsten oxide species exhibit a distorted tetrahedral structure at coverages of less than 1/3 monolayer. Samples left out in the air at room temperature exhibit octahedral site symmetry due to the coordination of water molecules to the surface tungsten oxide species, however this symmetry breaks down at 500 °C. Raman spectra of the W03/A1203 samples exhibit features attributed to W=O and W-0-W bonds, which is consistent with a deformed tetrahedral tungsten oxide environment. This research suggests that unbound and coupled tetrahedra of tungsten oxide occur on the surface. Tungsten oxide surfaces with coverages near to a monolayer reveal evidence in their XANES spectra of a significant proportion of the surface tungsten oxide sites having a deformed octahedral environment, even in the absence of coordinated water.

**Keywords:** XAFS, XRD, tungsten oxides, structure, hydrogen intercalation

## INTRODUCTION

All biological systems rely on so-called "inorganic" components for proper growth and maintenance. Most of these elements are often only found in very minute concentrations, yet this in no way minimises their importance. Many of these "trace elements," such as the transition metals vanadium, manganese, iron, cobalt, nickel, copper, zinc, molybdenum, and tungsten, have been demonstrated to play crucial roles in biological processes. Crystallography is an extremely potent method for elucidating not only the general molecular architecture of proteins but also the precise position of a single d-transition metal atom or a cluster of these atoms. Advances in protein crystallisation methods, the availability of increasingly powerful X-ray sources, the enhancement of detectors, and the massive growth in processing capacity for data collecting and analysis have

greatly expanded the scope and accuracy of protein crystallography. Thus, we are going toward a scenario in which, for a metalloprotein, not only do we anticipate a thorough structural characterisation, but also that this will be done for multiple derivatives, such as oxidised, reduced, inhibitor- or substrate analogue-bound, and site- or loop-directed mutations. Furthermore, there has been a significant development in the use of nuclear magnetic resonance (NMR) to determine protein structures in solution, and for metalloproteins, the existence of one paramagnetic centre is useful for the defining of the immediate surroundings of the metal Centre.

The structural data supplied by protein crystallography and NMR spectroscopy are beautiful and important, but they should only be seen as the first step toward a more in-depth exploration of the role(s) played by the r61e of the d-transition metal(s) in the biological activity of the enzyme. Determining the co-ordination of the metal atom(s) and how it changes between states in a redox-active protein and/or metalloenzyme is a crucial part of the systematic inquiry. Understanding the characteristics of metal centres in proteins requires knowledge of the local and global environments in which these centres are embedded. Currently, the best resolution that can be obtained using protein crystallography is inferior than that required to establish metal-ligand distances with an accuracy of greater than +oil. This level of uncertainty has profound chemical consequences. Since the accompanying Extended X-ray Absorption Fine Structure (EXAFS) may yield metal-ligand bond lengths to an accuracy of 20.03A, metal-edge X-ray Absorption Spectroscopy (XAS) is a viable option for probing metal centres in proteins. When both XAS and protein crystallography are used to investigate the same state of the system, the combined results are quite useful. X-ray absorption spectroscopy (XAS) is a flexible technology that may be employed independently of protein crystallography since it does not need crystallinity.

## LITERATURE REVIEW

**Upul Jayarathne (2014)** Mononuclear six-coordinate tungsten compounds were investigated using tungsten L-edge X-ray absorption spectroscopy. These compounds were typically found in an inert chloride and/or phosphine ligand environment. These compounds are distinguished by their L-edge spectra, which include those of [W(0)(PMe3)6], [W(II)Cl2(PMePh2)4, and [W(III)Cl2(dppe)2]. Some useful sources for understanding the electronic structure of tungsten compounds with redox-active ligands include (dppe = 1,2-bis(triphenylphosphine)ethane), [W(IV)Cl4(PMePh2)2], [W(V)(NPh)Cl3(PMe3)2], and [W(VI)Cl6]. These spectra are helpful for estimating the effective oxidation state of the metal since the estimated branching ratio of the L3,2-edges and the L1 rising-edge energy correspond well with metal Zeff. Take the X-ray absorption spectra at the L-edge for [W(IV)(mdt)2(CO)2] and [W(IV)(mdt)2(CN)2] as an example of a possible use of these reference spectra. (2-) (mdt(2-) = 1,2-dimethylethene-1,2-dithiolate), which shows that both compounds are effectively W(IV) species despite the mdt ligands occurring at different redox levels. Contextualizing the results with the spectra of known standards, particularly those with the same coordination number and metal ligand distances is essential when using metal L-edge XAS to analyse a molecule with an unknown formulation. Maximum and lowest metal Zeff values in the target species may be determined with the use of such spectra. Applying complementary physical methods, especially ligand K-edge XAS, to the data for interpretation. When interpreting data including powerful -acceptor ligands, such as CO, or -donor ligands, care must be taken to avoid incorrectly identifying the presence of these ligands. The combination of the electron-withdrawing/donating properties of these ligands and the short metal-ligand distances results in a broadening of the oxidation gap between the formal oxidation state and the metal Zeff, or, as in the case of [W(IV)(mdt)2(CO)2], a subtle effect is exerted to modulate the redox level of other ligands in the coordination sphere.

**Lulu Chen (2020)** In the context of renewable energy production, the necessity of developing efficient and low-cost electrocatalysts for water splitting cannot be overstated. Herein, Fe, Al-co-doped NiSe2 nanoparticles on reduced graphene oxide (Fe, Al-NiSe2/rGO) were synthesised as a bifunctional electrocatalyst for whole-house water splitting. As a result of a more robust electrical link between the foreign atoms and the host catalyst, adsorption energy of process intermediates may be increased by dual-cation doping. Al is removed from the crystal structure of the intended product by the alkaline wash, resulting to a rise in defects and, ultimately, a greater exposure of the active site. The Fe, Al-NiSe2/rGO catalyst shows high catalytic activity for both reactions, with an overpotential of 272 mV @ 10 for the OER in 1.0 M KOH and 197 mV @ 10 for the

HER in 0.5 M H2SO4. The voltage produced by a two-electrode electrolyzer with Fe, Al-NiSe2/rGO as the anode and cathode at a current density of 10 mA cm2 is only 1.70 V. Results from this study emphasise the synergistic impacts of the dual-cation co-doping effect and extra defects created by Al leaching, both of which boost water-splitting efficiency.

**Zhengkai Cao (2022)** As a game-changing method for increasing chemical material output, hydrocracking straight-run diesel has been touted. Diesel's hydrocracking behaviours were investigated to see how acidities and hydrogenation abilities of serial bifunctional catalysts impacted the reactions. Because of its high pore size and pore volume, Al2O3 may be an ideal support colony for spreading active metals, and the findings showed that the acidity of the catalysts increased in proportion to the quantity of Y zeolite added. Increasing Al2O3 content was also associated with improved hydrogenation performance. X-ray photoelectron spectra (XPS) and high-resolution transmission electron microscopy (HRTEM) results demonstrated that the NiW/AY-15 catalyst exhibited the highest percentage and dispersion degree of MoS2 active phases. Production of olefins from light naphtha, jet fuel, and improved diesel with high percentages of paraffins was found to be viable. Heavy naphtha, which is rich in aromatics and cyclones, might be used as a high-quality feedstock for the catalytic reforming unit. So as to get a higher output of chemicals, straight-run diesel was hydrocracked. The NiW/AY-15 catalyst was the most successful at hydrogenation, and as a result, its diesel hydrocracking product included a higher concentration of paraffins than that of the other catalysts tested. Finally, a kinetic model and reaction parameters of straight-run diesel hydrocracking were originally given based on the experimental results. Researchers found that straight-run diesel underwent hydrocracking in a pseudo-first-order form, based on their kinetic analysis.

**Penghui Yan (2021)** Over Ni-Fe, Ni-Mo, and Ni-W bimetallic catalysts, the hydrodeoxygenation (HDO) of guaiacol was investigated in a continuous-flow reactor. Both density functional theory (DFT) calculations and X-ray photoelectron spectroscopy (XPS) and temperature-programmed desorption (TPD) experiments showed that W and Fe significantly altered the electronic properties of Ni, suggesting that the formation of Ni-Fe and Ni-W alloys is thermodynamically favourable while the generation of a Ni-Mo alloy is unfavored. HDO was considerably enhanced by adding Mo or Fe to the 9 wt% Ni/BEA catalyst at a weight percent of 2.2%, but was retarded by adding W. Since the selectivity to hydrogenation products was not altered over the Ni-Fe/BEA catalyst compared to that of Ni/BEA during the hydrogenation of toluene, this suggests that the observed increase in guaiacol conversion was driven by the promotion of the direct hydrogenolysis of guaiacol to aromatics over Ni-Fe species. The TOFNi values for Ni/BEA and Ni-Mo/BEA were similar, suggesting that the increased Ni dispersion induced by Mo contributed to the higher hydrogenation and HDO rates of the Ni-Mo/BEA catalyst.

**Juliette Blanchard (2021)** Supported transition metal compounds have been identified as prospective catalysts for several processes by scientists in the fields of petroleum refining, energy, and environmental catalysis for decades. Improving the efficiency of catalytic materials by enhancing metal accessibility when supported by oxide carriers seems crucial if we are to make the most of Earth's limited supply of transition metals. The deposition of oxotungstates, followed by reduction at 600 °C under H2, greatly reduces Rh sintering in comparison to a W-free CeO2 support, allowing for the selective deposition of Rh on the CeO2 surface. Oxotungstates are regarded spacers because of their capacity to both decrease the number of available CeO2 nucleation sites and to physically separate the remaining sites. During the high-temperature reduction process, the Rh metallic phase may be protected from sintering by the oxotungstates. Experimental EXAFS measurements of extremely low coordination numbers of 4.0 0.2 are consistent with a variety of morphologies for sub-nanometric Rh clusters displaying restricted atomicity. Clusters of less than a few nanometers in size contain no more than five Rh atoms, as calculated from their coordination numbers and H2 chemisorption measurements. At 50 °C, the turnover frequencies of benzene hydrogenation were the same for both sub-nanometric Rh clusters and Rh nanoparticles of 2.5 nm.

## METHOD

Samples of tungsten oxide on y-alumina were prepared using the incipient wetness impregnation method by combining an aqueous ammonium metatungstate solution with the alumina powder. Samples were calcined in air at 500 or 950 degrees Celsius "C for 16 hours after being dried at 110 degrees Celsius. There were two WO concentrations tested on yalumina. At -30% WO on an alumina support, researchers observed that monolayer coverage of the surface species was 180 m2/g. Have your C calculated now.

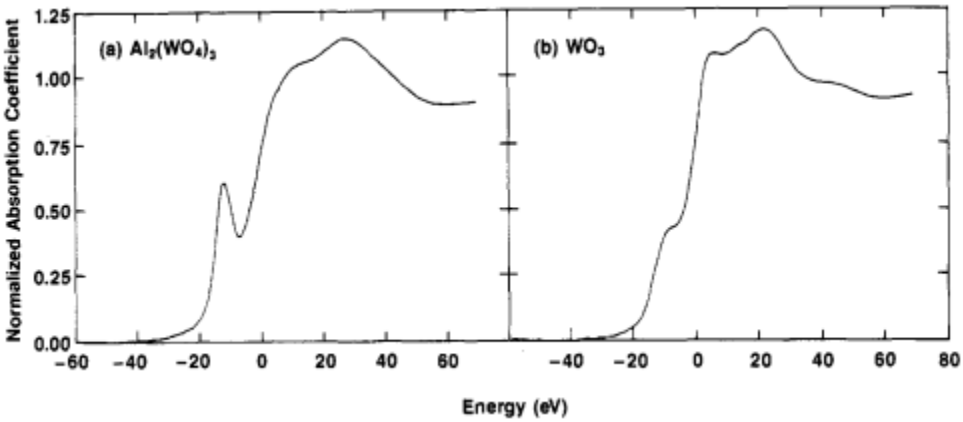


**Figure 1. Normalized tungsten L1-edge XANES spectra for the reference compounds (a) $AI_2$,($WO_3$,), and (b) $WO_3$,.**

The supported tungsten oxide phase in the samples was verified to be a surface species only by means of laser Raman spectroscopy. We were able to purchase from Ceric both conventional and deformed tetrahedral tungstates, as well as pure crystalline WO3 with its distorted comer-shared octahedra. Both the X-ray diffraction and laser Raman spectroscopy results confirmed what was already known about the crystal structures of the WO and A12(W04)3 samples. The X-ray absorption data was obtained at the Stanford Synchrotron Radiation Laboratory (SSRL) on beamline VII-3 using dedicated operation of SPEAR at 3 GeV and currents of 30-70 mA. Air-exposed samples' transmittance and fluorescence measurements were taken at ambient temperature. Microscopy using X-rays It was very similar to Stern and Heald's fluorescent-light detector. I8 Data were also obtained on samples that had been calcined at 500 OC in a mixture of 20% oxygen in helium to provide insight into what occurs when surface-coordinated water is eliminated. Samples were tested at 500 OC and room temperature in-situ, without being exposed to the elements.

The in-situ catalytic furnace used for these testing could measure both transmission and fluorescence simultaneously. 19 We were able to convert the XANES spectra to a WO-compatible energy scale by taking the first derivative of the edge spectrum. The pre-edge inflection point and the edge inflection point both contribute to peaks in the first derivative. To facilitate comparison, the XANES energies are shown in relation to the W L1 energy. The XANES spectra were normalised to unit step height by first fitting a quadratic polynomial spline to the EXAFS area of the data, then a linear function to the pre-edge data, then extrapolating both functions to zero energy and taking the difference. Laser Raman spectra were acquired using an Ar+ laser from Spectra-Physics, with incident energy measurements between 1000 and 1000 mW at the sample and a typical centre of the excited line at 514.5 nm. An OMA I11 optical multichannel analyzer from Princeton Applied Research, equipped with an amplified photodiode array cooled thermoelectrically to -30 OC, was utilised to evaluate the scattered light from the Spex Triplemate spectrometer.

## RESULTS AND DISCUSSION

h-WO3 and m-WO3 have different XRD peaks. For both the hexagonal and monoclinic lattice characteristics, the new data agrees well with the historical records. Further, the wide XRD peaks in c-simple WO3 represent the material's cubic XRD structure. Measurements show that intercalated m-WO3 exhibits two unique tetragonal phases, with tetragonal cell properties of a=5.238(2) and c=3.891(4) (Z=2) at x=0.23, and a=3.764(9)

and c=3.732(8) (Z=1) at x=0.35. These findings agree with the published research. According to previous research, hydrogen intercalation in h-WO3 modifies cell properties to a=7.364(0) and c=7.580(1) at x=0.35. With hydrogen intercalation in c-WO3, however, the cell parameter increases from a=3.70(4) at x=0.0 to a=3.74(8) at x=0.35.

All of the FTs and experimental XAFS signals for intercalated and non-intercalated molecules are shown in Figure 1. Intercalation with hydrogen significantly shifts the peaks up to 6 in the FTs of intercalated m-WO3 and h-WO3, but just slightly shifts the peaks in the FT of intercalated c-WO3. A deformed octahedron of oxygen (O1) atoms forms the initial coordination shell, and single-scattering events involving these atoms produce the first peak at R(W-O1)=1.7-2.3. The second peak is due to several scattering occurrences within the first shell of WO6 octahedra. The third peak, which corresponds to scattering from the second shell formed by tungsten (W2) atoms, has an amplitude that is heavily impacted by the strong focusing effect due to the oxygen atoms of the first shell and is reliant on the tilting W-O-W2 angle. Keep in mind that oxygens (O3), located in the third coordination shell, generate a wide range of the distances R(W-O3)=3.7-4.5, with a maximum at 4.2, and that they also make some contribution to the third peak. Tungsten's W4 atoms have a single-scattering signal at 5.3 eV, while the fifth-shell oxygen atoms in c-WO3 have a signal at 5.6 eV due to the presence of 30 eV O5 atoms.

Two methods, described above were used to model the experimental XAFS signals from the first shell. The values of N, R, and s2 were calculated using many multi-shell models (Table 1) that were developed using the XRD structural data. The interatomic W-O lengths were sorted by XRD, and the resulting groupings determined the fixed values for the coordination numbers N. The parameters R and s2 were used for the fitting process. The complete radial distribution functions (RDF) for the first shell were reconstructed without resorting to a model. (Fig. 2). X-ray diffraction data demonstrates that the octahedra of m-WO6 and WO3 are not equal due to the presence of twelve distinct W-O distances in the first shell of the former. Therefore, one must classify XRD and XAFS data in order to make meaningful comparisons (Table 1). Two models with three groups of oxygen atoms in each were used to assess the RDF, while a third model with two groups of oxygen atoms in each was also considered (Table 1). The RDF for the first shell of m-WO3 is shown in Fig. 2, wherein it varies widely from 1.7 to 2.3, with two peaks located at 1.75 and 2.1.

The W-O distances are found to be 1.77, 1.90, and 2.14 after fitting all three shells to the model of three groups of two oxygen atoms in each (2:2:2). Since the initial peak is so pronounced at 1.75, the DW factors for the shortest bonds are the lowest. The second peak at 2.1 is widened because the longest bonds have greater DW factors. The DW factor, s2 = 0.0084 2, for the central middle bonds in the three-shells model was also found to be quite high (Table 1). This helps to clarify why there are only two prominent maxima in the full RDF, at 1.75 and 2.1. (Fig. 2).

Similarly, to what was done with m-WO3, h-WO3 models containing either two (4:2) or three (2:2:2) oxygen atom groups were tested. Three-shells model is better than two-shells model in terms of fitting the data. The central and final peaks of RDFs are flattened because the DW factors of the middle and long bonds are higher inside the three-shells model. While the obtained data does not perfectly match the XRD structural model, it does show a stronger correlation in. Highly deformed WO6 octahedra are the outcome of three different sorts of W-O distances in the later model. In the hexagonal plane, there are two pairs of short and long W-O bonds. Additionally, there exist both short (1.80 ) and long (2.13 ) W-O bonds between the layers (I) and (2.18 ) W-O bonds between the layers (II). The RDFs (Fig. 2) of intercalated m- and h-WO3 oxides can be distinguished from the RDFs of nonintercalated compounds by virtue of the presence of an additional peak. The intercalated HxWO3 (m-WO3) data, when fit with a three-shells model and a cumulant model, yields a single large asymmetric Gaussian distribution.

The intercalated h-WO3 has a peak at 1.8 and a shoulder at 2.1, just like the h-WO3. The intercalated h-WO3 data performs better when fitted with a three-shells model (2:2:2), yielding three sets of distances at 1.81, 1.89, and 2.01. As a result, the hydrogen insertion gradually reduces the local deformation of the WO6 octahedra. The average W-O distances áR = 1.896 and 1.890 for c-WO3 and Hx(c-WO3), respectively, are quite

asymmetric, with a peak at 1.85. One asymmetric Gaussian peak is obtained from the one-shell fit using the model-independent technique and four cumulants. (Fig. 2). The X-ray diffraction pattern for c-WO3 and Hx(c-WO3) shows that they are both made up of the same kind of typical WO6 octahedron, with oxygen atoms in the 1.852 and 1.874 positions. When hydrogen is intercalated into c-WO3, the W-O distance in the first coordination shell is shortened by a small amount and the lattice parameter is increased by 0.04, as determined by XAFS (XRD data). The W-O-W tilting angle in c-WO3 seems to grow with hydrogen intercalation.

**Table 1. Best-fit values of distances R (in Å, ± 0.01 Å) and DW factors s 2 (in Å 2 , ± 30%) for the first coordination shell of tungsten obtained by multi-shell fit of XAFS spectra**

| Compound | XAFS | | | | XRD | | |
|---|---|---|---|---|---|---|---|
| | $N$ | $R$ (Å) | $\sigma^2$ | ε x $10^{-4}$ | $N$ | $\langle R \rangle$ | Δ |
| c-$ReO_3$ | 6 | 1.86 | 0.0031 | 25 | 6 | 1.87 | 0.01 |
| c-$WO_3$ | 6 | 1.89[a] | 0.013 | 19 | 6 | 1.85[b] | -0.04 |
| $H_x$(c-$WO_3$) | 6 | 1.89[a] | 0.015 | 33 | 6 | 1.87[b] | -0.02 |
| m-$WO_3$ | 3 | 1.79 | 0.0032 | 14 | 3 | 1.79 | 0.00 |
| | 3 | 2.09 | 0.011 | | 3 | 2.07 | -0.02 |
| m-$WO_3$ | 2 | 1.77 | 0.0010 | 7 | 2 | 1.75 | -0.02 |
| | 2 | 1.91 | 0.0084 | | 2 | 1.90 | -0.01 |
| | 2 | 2.15 | 0.0042 | | 2 | 2.14 | -0.01 |
| $H_x$(m-$WO_3$) | 6 | 1.92[a] | 0.017 | 78 | 6 | 1.88[b] | -0.04 |
| $H_x$(m-$WO_3$) | 2 | 1.82 | 0.0017 | 27 | 4 | 1.87[b] | 0.05 |
| | 2 | 1.93 | 0.0048 | | 2 | 1.88[b] | -0.05 |
| | 2 | 2.10 | 0.0071 | | | | |
| h-$WO_3$ | 4 | 1.82[a] | 0.084 | 74 | 4 | 1.89[b] | 0.07 |
| | 2 | 2.11 | 0.060 | | 2 | 1.95[b] | -0.16 |
| h-$WO_3$ | 2 | 1.78 | 0.0014 | 8 | 2 | | |
| | 2 | 1.94 | 0.0078 | | 2 | 1.95[b] | 0.01 |
| | 2 | 2.15 | 0.0080 | | 2 | | |
| $H_x$(h-$WO_3$) | 4 | 1.84 | 0.0073 | 36 | 4 | | |
| | 2 | 1.99 | 0.0176 | | 2 | 1.89[b] | -0.10 |
| $H_x$(h-$WO_3$) | 2 | 1.81 | 0.0030 | 8 | 2 | | |
| | 2 | 1.89 | 0.0057 | | 2 | 1.89[b] | 0.00 |
| | 2 | 2.04 | 0.0130 | | 2 | | |

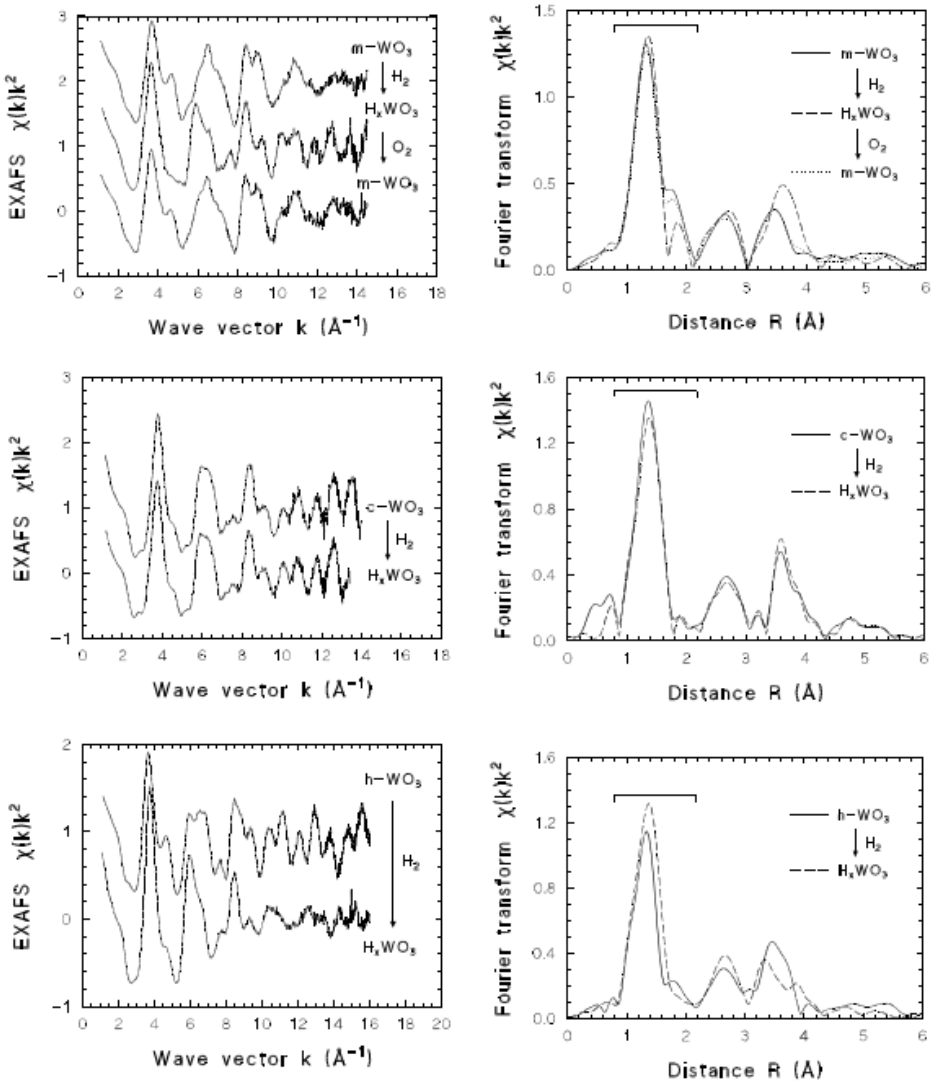


**Figure. 1. Experimental XAFS spectra measured at the W L3-edge in m-WO3, c-WO3 and h-WO3**

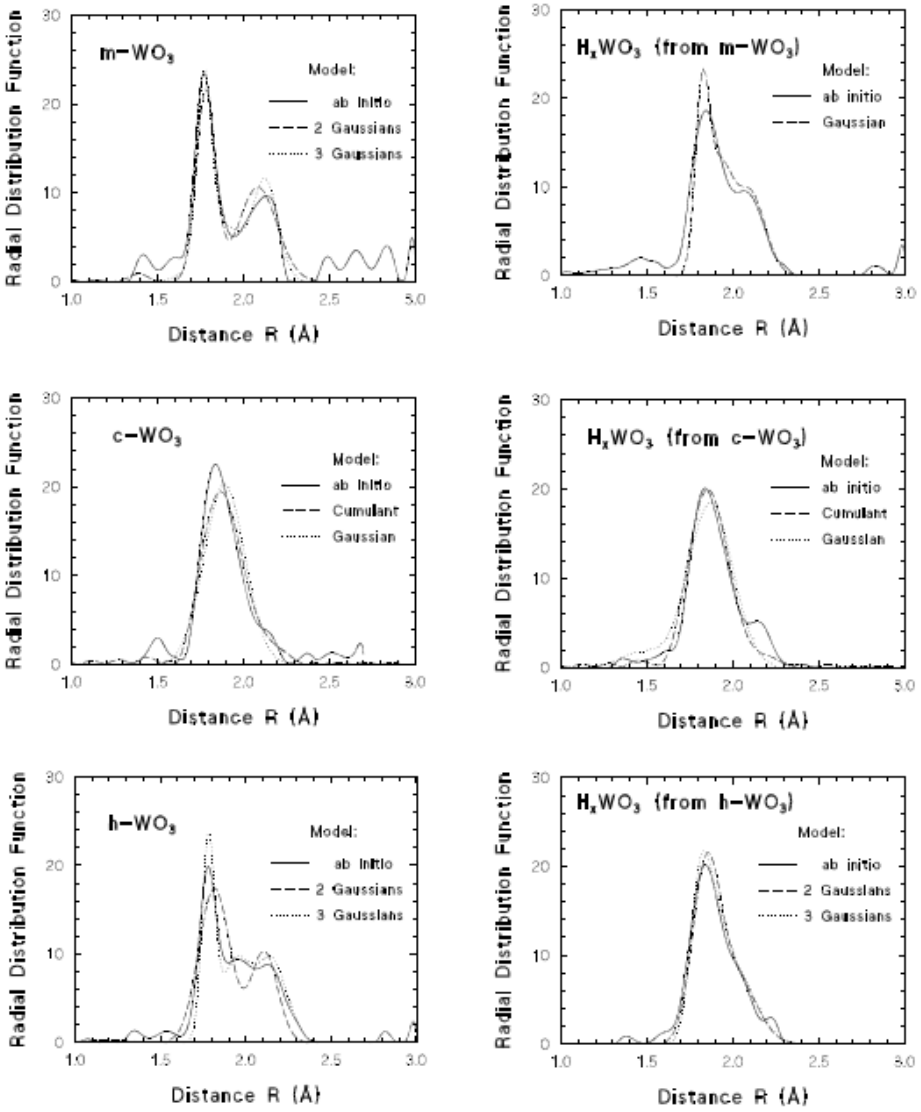


**Figure. 2. The RDF's for the first shell of tungsten in tungsten oxides**

## CONCLUSIONS

Gains are being made in the field of coordination chemistry, specifically as it relates to the study of d-transition metal ions in proteins. When we combine the results of crystallographic and spectroscopic investigations with information acquired from studies of relevant co-ordination chemicals, we get a better understanding of how chemical activity is controlled at transition metal centres in proteins to fulfil particular biological tasks. Hydrogen intercalation in both m-WO3 and h-WO3 has been extensively studied using a wide variety of methods. In the beginning, m-WO3 and h-WO3 were measured by x-ray diffraction (XRD) and neutron diffraction to establish a baseline for tungsten bronzes HxWO3 with x ranging from 0 to 0.6. However, as far as we are aware, hydrogen intercalation in cWO3 has never been studied. In the absence of coordinated water, a spectrum is seen that demonstrates tetrahedral distortion of surface species at coverages below monolayer. Air-exposed samples of water molecules produce octahedral site symmetry, however this is broken when the samples are heated to 500 degrees Celsius. Characteristics attributed to W=O and W-0-W bonds are seen in the laser Raman spectra of WO3/A1203 samples, which are consistent with a deformed tetrahedral tungsten environment. For this reason, we suggest that the tungsten oxide on the alumina surface takes the form of both free and bound tetrahedra.

**REFERENCES**


1. Jayarathne, Upul & Chandrasekaran, Perumalreddy & Greene, Angelique & Mague, Joel & DeBeer, Serena & Lancaster, Kyle & Sproules, Stephen & Donahue, James. (2014). X-ray Absorption Spectroscopy Systematics at the Tungsten L-Edge. Inorganic chemistry. 53. 10.1021/ic500256a.

2. Lulu Chen, Haeseong Jang, Min Gyu Kim, Qing Qin, Xien Liu, Jaephil Cho. Fe, Al-co-doped NiSe 2 nanoparticles on reduced graphene oxide as an efficient bifunctional electrocatalyst for overall water splitting. Nanoscale 2020, 12 (25) , 13680-13687. https://doi.org/10.1039/D0NR02881A

3. Zhengkai Cao, Xia Zhang, Jinlin Mei, Rong Guo, Ziming Wu, Shuandi Hou, Shaozhong Peng, Siqiang Fan, Chong Peng, Aijun Duan. Hydrocracking Straight-Run Diesel into High-Value Chemical Materials: The Effect of Acidity and Kinetic Study. Industrial & Engineering Chemistry Research 2022, 61 (25) , 8685-8697. https://doi.org/10.1021/acs.iecr.2c00262

4. Penghui Yan, Xinxin Tian, Eric M. Kennedy, Olga Petrovna Tkachenko, Michael Stockenhuber. Influence of Promoters (Fe, Mo, W) on the Structural and Catalytic Properties of Ni/BEA for Guaiacol Hydrodeoxygenation. ACS Sustainable Chemistry & Engineering 2021, 9 (46) , 15673-15682. https://doi.org/10.1021/acssuschemeng.1c06266

5. Jeffrey T. Miller, Neil M. Schweitzer, Mimoun Aouine, Philippe Vernoux, Abdelmalik Boufar, Juliette Blanchard, Jean-Marc Krafft, Christophe Méthivier, Céline Sayag, Frédéric Ser, Mickaël Sicard, Cyril Thomas. Successive Strong Electrostatic Adsorptions of [RhCl6]3– on Tungstated-Ceria as an Original Approach to Preserve Rh Clusters From Sintering Under High-Temperature Reduction. The Journal of Physical Chemistry C 2021, 125 (45) , 25094-25111. https://doi.org/10.1021/acs.jpcc.1c07644

6. Gustavo A. S. Alves, Higor A. Centurion, Julio R. Sambrano, Mateus M. Ferrer, Renato V. Gonçalves. Band Gap Narrowing of Bi-Doped NaTaO3 for Photocatalytic Hydrogen Evolution under Simulated Sunlight: A Pseudocubic Phase Induced by Doping. ACS Applied Energy Materials 2021, 4 (1) , 671-679. https://doi.org/10.1021/acsaem.0c02547

7. Wen Chang, Bo Qi, Yu-Fei Song. Step-by-Step Assembly of 2D Confined Chiral Space Endowing Achiral Clusters with Asymmetric Catalytic Activity for Epoxidation of Allylic Alcohols. ACS Applied Materials & Interfaces 2020, 12 (32) , 36389-36397. https://doi.org/10.1021/acsami.0c10207

8. Yifei Liu, Lifeng Zhang, Florian Göltl, Madelyn R. Ball, Ive Hermans, Thomas F. Kuech, Manos Mavrikakis, James A. Dumesic. Synthesis Gas Conversion over Rh-Mn-WxC/SiO2 Catalysts Prepared by Atomic Layer Deposition. ACS Catalysis 2018, 8 (11) , 10707-10720. https://doi.org/10.1021/acscatal.8b02461

9. Ning Zhang, Chen Chen, Yule Chen, Gen Chen, Chengan Liao, Bo Liang, Jisheng Zhang, An Li, Baopeng Yang, Zhihe Zheng, Xiaohe Liu, Anqiang Pan, Shuquan Liang, Renzhi Ma. Ni2P2O7 Nanoarrays with Decorated C3N4 Nanosheets as Efficient Electrode for Supercapacitors. ACS Applied Energy Materials 2018, 1 (5) , 2016-2023. https://doi.org/10.1021/acsaem.8b00114

10. Chen Chen, Ning Zhang, Yulu He, Bo Liang, Renzhi Ma, and Xiaohe Liu . Controllable Fabrication of Amorphous Co—Ni Pyrophosphates for Tuning Electrochemical Performance in Supercapacitors. ACS Applied Materials & Interfaces 2016, 8 (35) , 23114-23121. https://doi.org/10.1021/acsami.6b07640

11. Michal J. Mleczko, Runjie Lily Xu, Kye Okabe, Hsueh-Hui Kuo, Ian R. Fisher, H.-S. Philip Wong, Yoshio Nishi, and Eric Pop . High Current Density and Low Thermal Conductivity of Atomically Thin Semimetallic WTe2. ACS Nano 2016, 10 (8) , 7507-7514. https://doi.org/10.1021/acsnano.6b02368

12. Jian Gao, Baichang Li, Jiawei Tan, Phil Chow, Toh-Ming Lu, and Nikhil Koratkar . Aging of Transition Metal Dichalcogenide Monolayers. ACS Nano 2016, 10 (2) , 2628-2635. https://doi.org/10.1021/acsnano.5b07677

13. Kai Liu, Zhixiao Yao, and Yu-Fei Song . Polyoxometalates Hosted in Layered Double Hydroxides: Highly Enhanced Catalytic Activity and Selectivity in Sulfoxidation of Sulfides. Industrial & Engineering Chemistry Research 2015, 54 (37) , 9133-9141. https://doi.org/10.1021/acs.iecr.5b02298

14. Martin E. McBriarty, Gavin P. Campbell, Tasha L. Drake, Jeffrey W. Elam, Peter C. Stair, Donald E. Ellis, and Michael J. Bedzyk . Atomic-Scale View of VOX–WOX Coreduction on the α-Al2O3 (0001) Surface. The Journal of Physical Chemistry C 2015, 119 (28) , 16179-16187. https://doi.org/10.1021/acs.jpcc.5b04802

15. Mauro Epifani, Raül Díaz, Carmen Force, Elisabetta Comini, Marta Manzanares, Teresa Andreu, Aziz Genç, Jordi Arbiol, Pietro Siciliano, Guido Faglia, and Joan R. Morante . Surface Modification of TiO2 Nanocrystals by WOx Coating or Wrapping: Solvothermal Synthesis and Enhanced Surface Chemistry. ACS Applied Materials & Interfaces 2015, 7 (12) , 6898-6908. https://doi.org/10.1021/acsami.5b00632